Sensors and Materials, Vol. 38, No. 1 (2026) 55–70
MYU Tokyo

S & M 4283

Fabrication of a Novel Circularly Polarized Microstrip Patch Antenna Sensor and Its Bidirectional Strain Monitoring Performances

Liguang Liu,[1] Jianlin Luo,[1*] Kwok L. Chung,[2**] Yang Liu,[3] and Aiqi Cui[1]

[1]School of Civil Engineering, Marine Environmental Concrete Technology Engineering Research Center of Ministry of Education, Qingdao University of Technology, Qingdao 266520, P. R. China
[2]School of Intelligent Manufacturing and Electrical Engineering, Guangzhou Institute of Science and Technology, Guangdong 510540, P. R. China
[3]School of Transportation Science and Technology, Harbin Institute of Technology, Harbin 150090, P. R. China

(Received September 11, 2025; accepted November 28, 2025)

Keywords: structure monitoring, antenna sensor, microstrip patch antenna, circular polarization, bidirectional strain monitoring

Antenna sensors designed on the basis of the antenna principle have both sensing and signal transmission functions, which can effectively solve the wiring complexity problem and reduce installation cost from traditional sensors in structural monitoring. In this study, we designed a microstrip patch antenna sensor (MPAS) combined with theoretical deduction and simulation analysis. The radiation patch of the antenna was slotted to resonate within the target frequency band, achieving a reflection coefficient (S_{11}) of less than −10 dB and excellent circular polarization, ensuring superior antenna performances. A strain acquisition instrument was employed to acquire the bidirectional strains (ε_x, ε_y) of a cantilever beam end surface-attached MPAS, while the input impedance (Z) and S_{11} of the MPAS were measured using a vector network analyzer, whereby the bidirectional strain sensitivity (GF_x, GF_y) and linear stability of the MPAS were obtained by fitting the relationship between ε_x, ε_y and Z_{min} or S_{11}. The results showed that the MPAS can sense well ε_x and ε_y. Fitting the normalized S_{11} and ε_x, ε_y yields high GF_x and GF_y values of 141 and −140 ppm/με with superior goodness-of-fit values of 0.978 and 0.979, respectively, which indicate a sensitivity much higher than those of conventional strain sensors.

1. Introduction

Steel structures are widely used in civil engineering projects because of their reliable material properties, rapid construction capabilities, and cost-effectiveness.(1) However, owing to static/cyclic loads and exposure to harsh environments, metallic structural components in infrastructure sustain damage in service.(2) In severe cases, it may lead to major safety accidents, posing a significant threat to people's lives and property safety.(3) Structural health monitoring

*Corresponding author: e-mail: lawjanelim@qut.edu.cn
https://doi.org/10.18494/SAM5929

ISSN 0914-4935
https://myukk.org/

(SHM) systems effectively prevent the occurrence of disasters by continuously monitoring and recording data to identify damage-induced changes.[4] Common sensors for SHM are piezoresistive, piezoelectric, capacitive, optic fiber, and so forth. Piezoresistive sensors transform the structural deformation/strain into resistivity variations to reflect structural health.[5] Jiang *et al.* developed a nanomaterial-modified piezoresistive sensor.[6] This sensor utilizes the high porosity of melamine sponge (MS) to provide a large number of attachment surfaces for nanoparticles. It is constructed by intertwining black phosphorus-gold nanocomposites (BP-AuNCs) with MS, enabling strain monitoring in the strain range of 0–90%. Piezoelectric sensors monitor structural dynamic signals using polarized dielectric materials that generate electrical signals under mechanical stress.[7] Jiang *et al.* developed a novel 0-3 PZT/silicone rubber resin piezoelectric composite sensor (PZT/SR-FPCS).[8] The strain sensitivity of the PZT/SR-FPCS ranges from 8.59 to 9.81 mV/με, and its yield failure strain reaches 7.22%. Capacitive pressure sensors are applications of the parallel-plate capacitance principle. A change in distance between conductors leads to a change in capacitance. Capacitive sensors can convert pressure stimuli into changes in capacitance to achieve the strain monitoring of structures.[9] Zhang *et al.* developed a self-powered wireless pressure-sensing system (SP-WPSS) based on a capacitive triboelectric pressure sensor (CTPS).[10] The SP-WPSS combines porous ecoflex film/CNT composite dielectric layers with copper foil electrodes, through integration with LC resonant circuits, the open-circuit voltage reaches 1010.6 V, and the CTPS fabricated based on this achieves a sensitivity of 78.78 V/kPa. Fiber optic sensors rely on environmentally induced alterations in optical parameters (intensity, phase, and amplitude) during light propagation.[11] Lin *et al.* designed an optical sensor for measuring tensile strain using a diffraction grating and a surface plasmon resonance interferometer.[12] They used the heterodyne interferometry technique to precisely measure the phase change and characterize the structural strain. This sensor achieved a measurement resolution of 0.52 με and a sensitivity of 0.58 °/με within a dynamic range of 10 με.

It can be seen that the above sensors require complex wiring arrangements, complex chemical synthesis, and relatively high manufacturing cost. Undoubtedly, this increases the complexity of the SHM system and raises the installation cost of the sensors.[13,14] A microstrip patch antenna mainly consists of three parts: a dielectric substrate, a radiation patch, and a ground plane. Their simple structure endows them with features such as a low profile, small size, light weight, strong conformal ability, and flexible design.[15–17] By changing the shape and size of the radiation patch, the position of the feeding point, the characteristics and thickness of the substrate material, and so forth, the operating frequency band, input impedance, and polarization mode of the antenna can be easily adjusted. The microstrip patch antenna sensor (MPAS) made on the basis of the microstrip patch antenna uses the antenna as a strain-sensing element, integrating signal acquisition and transmission. This can reduce the size of the sensor system and avoid the use of peripheral circuits, therefore reducing the complexity and cost of the SHM system.[18,19]

The operating principle of the MPAS lies in converting dimensional variations of radiation patches induced by strain into alterations of antenna intrinsic characteristics such as resonant frequency, reflection coefficient, and input impedance. By monitoring these parameter changes and establishing their variation patterns, structural strain can be inversely deduced for SHM. He *et al.* developed an MPAS based on the strain-induced resonant frequency shift mechanism.[20]

The MPAS is composed of a polyimide film dielectric substrate and a rolled copper radiation patch. The two resonant frequencies of the MPAS are 5.67 and 6.77 GHz, with a maximum sensitivity of 22.63 kHz/με and a goodness-of-fit exceeding 0.92. However, the thin dielectric substrate and narrow microstrip line caused concentrated current distribution and significant conductor loss. However, the high-impedance microstrip line faced implementation challenges in engineering practice. Ge *et al*. developed a rectangular MPAS through simulation and experimental validation, with resonant frequencies of 2.70 and 4.05 GHz, respectively. They had established the correlation between structural strain and resonant frequency shift, having achieved a maximum sensitivity of 46.8 kHz/με.[21] Their work confirmed that larger radiation patch dimensions or higher resonant frequencies enhance the sensitivity of the MPAS. However, its resonant frequency exhibits an inverse relationship with radiation patch dimensions, necessitating a balanced consideration of both parameters in design optimization for smart materials and SHM applications. Lopato and Herbko investigated a circular MPAS capable of the simultaneous detection of strain and direction through the analysis of two resonant frequencies.[22] The sensor established the directional characteristic curve of the MPAS for the first time, realizing the simultaneous monitoring of strain magnitude and direction. However, the monitoring of strain direction by the sensor requires relatively complex calculations, and the strain magnitude in the $\alpha = 60°$ direction needs to be analyzed in combination with two resonant frequencies. Xu *et al*. used a main antenna to monitor structural cracks and two antennas placed in different directions to monitor structural strain, creating an antenna sensor array.[23] The sensor achieved multi-directional structural strain and crack monitoring. However, the abovementioned sensors are relatively large, with a maximum sensitivity of only 1.95 kHz/με, and they can only monitor cracks at the location of the antenna. Li *et al.* proposed an antenna sensor that can be embedded in concrete as smart aggregates.[24] The radiation patch of the sensor consists of a bottom main patch and an overlapping subpatch, which significantly improves the deformation adaptability of the sensor, thereby enabling a wider range of strain monitoring. However, this design can only achieve the length variation of the unilateral radiation patch, so it only supports unidirectional strain monitoring. Weng *et al*. utilized the mechanical stability, corrosion resistance, and good ductility of graphene to fabricate a graphene radiation patch antenna sensor by fixing graphene on a PET dielectric substrate via spray adhesive.[25] This sensor exhibits high flexibility and still maintains excellent linearity when detecting large strains up to 65000 με. However, compared with metal structure antenna sensors, the process of manufacturing this sensor is more complex. These studies show that existing antenna sensors still face challenges such as limited strain characterization methods and reliance on complex computations for multi-directional strain monitoring.

In this study, the MPAS was diagonally fed and the radiation patch was slotted to perturb the surface current, generating two vertical current modes with a 90° phase difference.[26] This design tunes the operating frequency band to the target range, achieves the antenna's circular polarization, and further enables bidirectional strain monitoring. Through experimental analysis, we fitted the relationship between the strain of the cantilever and the characteristics (such as S_{11} and Z_{min}) of the circularly polarized MPAS to enable the simplified monitoring of both strain magnitude and direction. Then, the data measured in the experiments were sorted out and a

sensor with both strain monitoring and signal transmission capabilities was obtained. This sensor can be used for the strain monitoring of complex steel structures to solve the problems of difficult wiring under complex stress conditions and the need for multiple sensors to detect variable strain direction.

2. Experiment

2.1 Determination method for radiation patch dimensions for antenna sensors

The transmission line model theory equates the rectangular patch antenna to a section of the transmission line, making the design of rectangular microstrip patch antennas more intuitive and convenient.[27,28] Therefore, in this study, the transmission line theory for design is adopted. In the transmission line model, the rectangular radiation patch of the antenna is regarded as a conducting strip with length (L) and width (W). First, the W of the radiation patch is determined from the initially set resonant frequency according to Eq. 1.

$$W = \frac{c}{2f_p}\left(\frac{\varepsilon_r + 1}{2}\right)^{-\frac{1}{2}} \tag{1}$$

Here, c is the speed of light in vacuum and f_p is the preliminary design resonant frequency of the antenna.

Owing to fringe field effects at the patch edges, the electric field is distributed in the dielectric substrate and air medium at the same time. To account for dielectric inhomogeneity, the effective permittivity ε_{eff} is calculated as

$$\varepsilon_{eff} = \frac{\varepsilon_r + 1}{2} + \frac{\varepsilon_r - 1}{2\sqrt{1 + 12\frac{H}{W}}}, \tag{2}$$

where ε_r is the dielectric constant of the dielectric substrate and H is the dielectric substrate thickness.

Because the electric field of the patch antenna exists in the air at both the dielectric base and the edge of the radiation patch, the theoretical electrical dimensions of the radiation patch exceed its geometrical dimensions.[29] Consequently, the effective length of the radiation patch (L_{eff}) is the sum of its L and the compensation length (ΔL). The empirical Eqs. (3) and (4) are given as

$$\Delta L = 0.412H\frac{\left(\varepsilon_{eff} + 0.3\right)\left(\frac{W}{H} + 0.264\right)}{\left(\varepsilon_{eff} - 0.528\right)\left(\frac{W}{H} + 0.816\right)}, \tag{3}$$

$$L_{eff} = \frac{\lambda}{2} = L + 2\Delta L, \tag{4}$$

where λ is the guided wavelength within the dielectric substrate. The calculation of λ is governed by the following relationship expressed as

$$\lambda = \frac{c}{f\sqrt{\varepsilon_{eff}}}. \tag{5}$$

The optimized resonant frequency (f) is derived from the relationship expressed as

$$f = \frac{1}{2L_{eff}\sqrt{\varepsilon_{eff}}\sqrt{\mu_0\varepsilon_0}} = \frac{c}{2\sqrt{\varepsilon_{eff}}\left(L + 2\Delta L\right)}, \tag{6}$$

where μ_0 and ε_0 are the permeability and permittivity of free space, respectively.

2.2 Materials and optimization of dimensions

The MPAS primarily comprises a radiation patch, a dielectric substrate, and a ground plane (Fig. 1). The conformal integration of the antenna with the host structure means that structural strain will alter the dimensions of these core components, consequently shifting the fundamental parameters of the MPAS. Although increasing the thickness of the dielectric layer can enhance bandwidth and radiation efficiency, thinner dielectric layers maintain superior conformability with a structure without sacrificing radiation performance.[30] Therefore, Rogers 5880 laminate (RT/duroid5880) was selected as the dielectric substrate for the antenna sensor. The substrate dimensions are 304.8 mm × 228.6 mm × 0.787 mm (length × width × thickness). Both surfaces are covered with 17.5 μm copper foil. The key material properties of the Rogers 5880 substrate are summarized in Table 1.

The Industrial, Scientific, and Medical (ISM) band refers to specific radio frequency ranges allocated by national authorities primarily for non-telecommunication applications in industrial, scientific, and medical fields.[31] The operational frequency of the antenna sensor has been

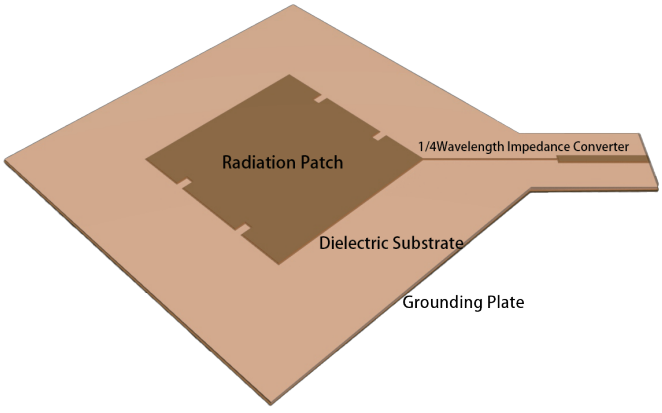

Fig. 1. (Color online) Composition of MPAS.

Table 1
Material properties of Rogers 5880 laminate.

Dielectric constant	Loss tangent (N/A)	Tensile modulus (MPa)	Ultimate strain (%)
2.2 ± 0.002	0.0004	1070	6.0
Density (g/cm^3)	Copper clad type	Cu foil peel strength (N/mm)	Poisson's ratio
2.2	Electrolytic Copper	0.1	0.3

initially determined as 2.45 GHz, which falls within the internationally shared ISM frequency spectrum. Therefore, we designed the resonant frequency of the MAPS to be around 2.45 GHz.

On the basis of Eqs. 1–6 and Table 1, the radiation patch size was initially determined to be 40 mm. To accommodate the microstrip line and quarter-wavelength impedance transformer along the length direction and reduce the effect of the magnetic permeability of the measured metal on the MPAS, both the dielectric substrate and the ground plane are designed to be twice the size of the radiation patch, with a width of 80 mm. Therefore, the above formula does not consider the effect of the magnetic permeability of the measured metal on the MPAS. Circular polarization was achieved through the diagonal alignment of the microstrip feed line relative to the patch geometry, followed by the slotting technique for performance optimization. By controlling the size of the radiation patch and the position of the feeding point, and slotting the radiation patch, the resonant frequency was stabilized within the target frequency range, and excellent radiation characteristics were maintained. Because the slot position is symmetrical, parametric optimization in the CST Studio Suite™ focused on three variables: slot width (W_s), slot length (L_s), and slot position (P_s). Electromagnetic simulation results showed optimized parameters: L_s = 2.5 mm, W_s = 1.5 mm, and P_s = 10 mm.

2.3 Precision fabrication and modular integration of antenna sensors

We exported the antenna planar model that was designed and optimized in CST Studio Suite as a DXF file, and imported it into AutoCAD software to close its contour lines and obtain the planar model of the MPAS (Fig. 2). The Rogers 5880 substrate was secured on the working platform of the LPKF ProtoMat S36 laser engraving machine (LPKF Laser & Electronics AG, Shanghai) using masking tape. Then, the closed planar model was transferred to the LPKF CircuitPro 2.3 control software integrated with the engraving system, and the material parameters and dielectric substrate type were configured.

After cutting was completed, the folded part of the antenna sensor was covered and protected with 100% cotton nonwoven fabric. With pliers, the microstrip line of the planar sensor was folded into a 90° L-shape to facilitate connection with the radio frequency (RF) cable, thus enabling sensor installation at any position on the surface of the experimental device.[32] Finally, a soldering iron was used to solder the front end of the microstrip line to the sub-miniature A (SMA) RF connector to ensure secure contact between the microstrip feed ground plate and the SMA flange, as well as between the microstrip feed front end and the SMA connector pin. A multimeter is employed to test the electrical conductivity at the connection points. The cutting, folding, and soldering processes of the antenna sensor are shown in Fig. 3.

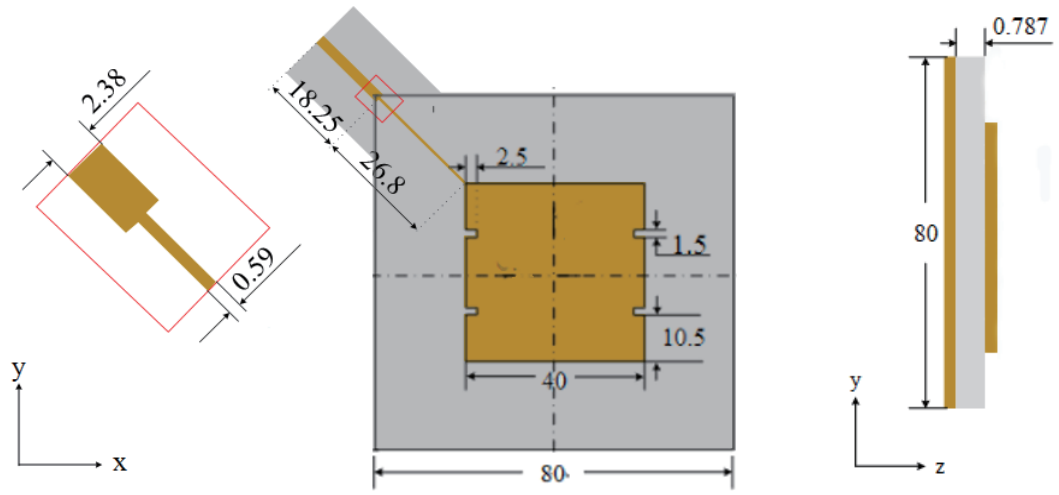

(a) (b)

Fig. 2. (Color online) Microstrip patch antenna sensor: (a) top and (b) side views (unit: mm).

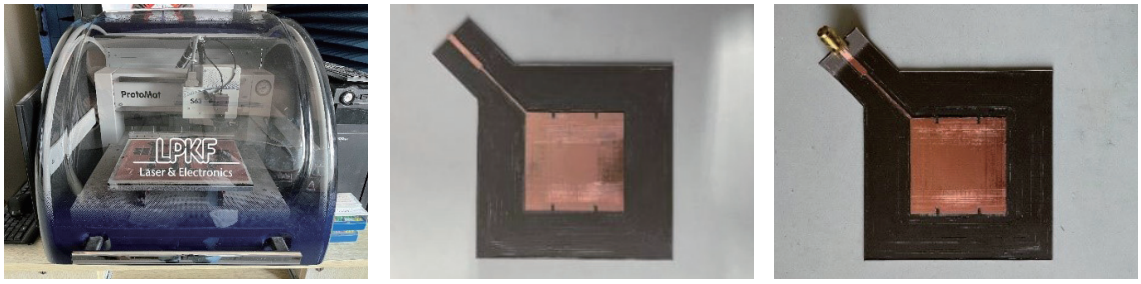

(a) (b) (c)

Fig. 3. (Color online) Antenna sensor manufacturing process: (a) engraving with a laser engraving machine, (b) a plan after carving, and (c) a folded and welded planar sensor.

3. Antenna Sensor Performance Test

3.1 Electromagnetic performance test

We employed a vector network analyzer (KEYSIGHT N5222A PNA, Keysight Technologies, model, USA) to conduct the electromagnetic performance test of the MPAS under various frequencies after 1 h preheating. We calibrated the PNA using the electronic calibration kit (Keysight N4691B, USA) to eliminate errors between the equipment and RF connections, and the setup is shown in Fig. 4(a).

The measured input impedance (Z) characteristics of the MPAS are shown in Fig. 4(b). The Z curve exhibits two distinct peaks: the TM_{10} mode resonant frequency (f_{10}) at 2.402 GHz and the TM_{01} mode resonant frequency (f_{01}) at 2.458 GHz. The resonant frequency f_m corresponding to the minimal Z (Z_{min}) is 2.438 GHz. This clearly demonstrates that the MPAS exhibits distinct adjacent orthogonal dual-mode characteristics.

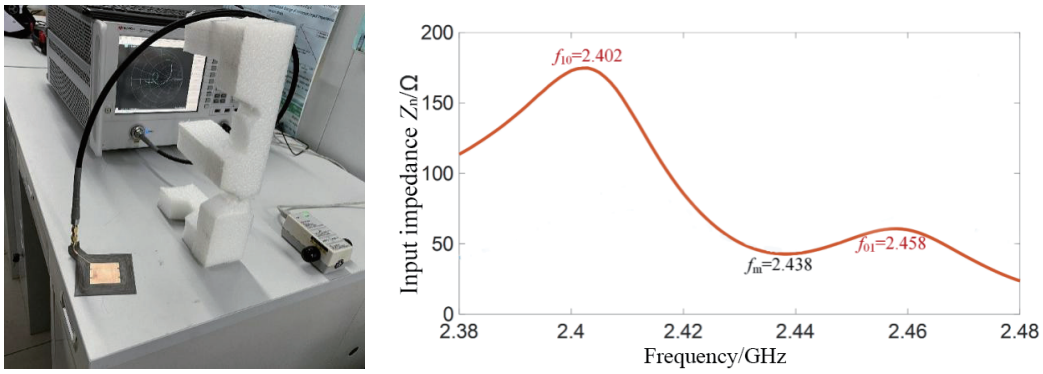

(a) (b)

Fig. 4. (Color online) (a) Electromagnetic performance test setup. (b) Input impedance of the MPAS.

3.2 Strain sensing performance test

An AL1060-type aluminum beam with dimensions of 480 × 120 × 1.5 mm^3 was sanded at 45° using 240-grit sandpaper. The antenna sensor was adhered to one end of the aluminum beam using 502 Super Glue adhesive with a length of 40 mm from the edge. A 5 mm × 3 mm glue-based foil strain gauge (BX120 × 5AA) was similarly adhered next to the antenna sensor and on the opposite side of the cantilever beam at a position geometrically corresponding to the center of the MPAS. The assembly was wrapped with polyethylene film to squeeze out air bubbles, left to dry in a ventilated area, and the film was removed after drying. A C-clamp was used to fix the side of the beam with the sensor 20 mm from the edge.

To test the bidirectional strain monitoring capability of the MPAS, tensile and compressive strain tests were conducted along the *x*- and *y*-directions of the MPAS, respectively. Since the load can only be applied along the length direction of the cantilever beam, two sets of experimental devices need to be designed, and the *x*- and *y*-directions of the MPAS were aligned along the length direction of the cantilever beam (Fig. 5). The experimental device was turned upside down when measuring the responses of the MPAS under compressive strains.

During the experiment, eight weights (100 g each) were hung one by one at the end of the aluminum beam to generate various strains; the corresponding theoretical strain amplitude ranged from 0 to 960 με at 120 με intervals. A strain acquisition instrument (DH5922D type, Donghua Testing Company, Jiangsu, China) and the abovementioned PNA were used to collect strain data and electromagnetic parameters for eight sets of tensile and compressive loads in each direction, with 10 repeats per set. The experimental setup and real image of the MPAS attached to the beam for strain monitoring are shown in Fig. 6.

4. Results and Discussion

4.1 Strain sensing performances with input impedance

Figure 7 shows the *Z* values of the MPAS under different *x*-direction strains. Figure 7(a) demonstrates that as tensile strain increases, the resonant frequency f_{10} corresponding to the

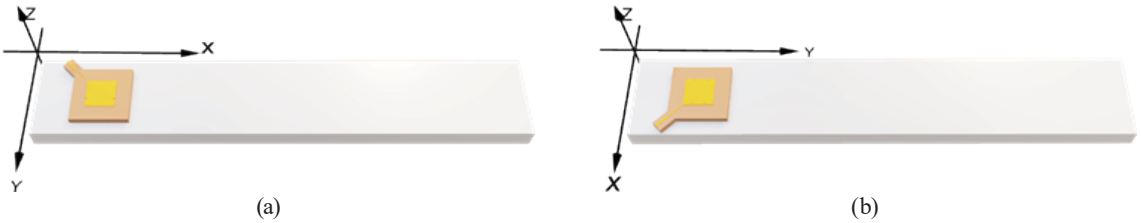

(a) (b)

Fig. 5. (Color online) Schematic diagram of MPAS installation directions: (a) x- and (b) y-directions.

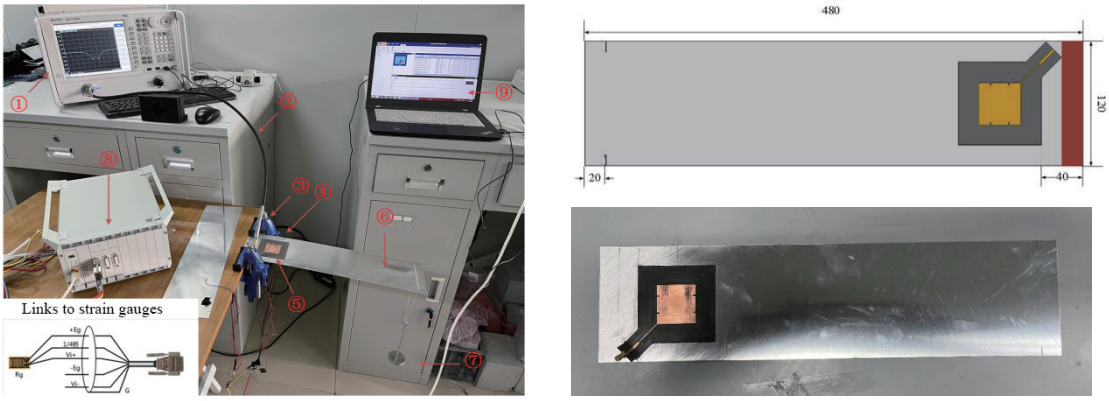

(a) (b)

Fig. 6. (Color online) (a) Experimental setup for strain monitoring of cantilever beam with MPAS (1- PNA; 2- RF cable; 3- C-clamp; 4- strain gauge; 5- MPAS; 6- cantilever beam; 7- weights; 8- strain collection instrument; 9- strain collection control terminal). (b) Dimensions and real image of cantilever beam with sensor.

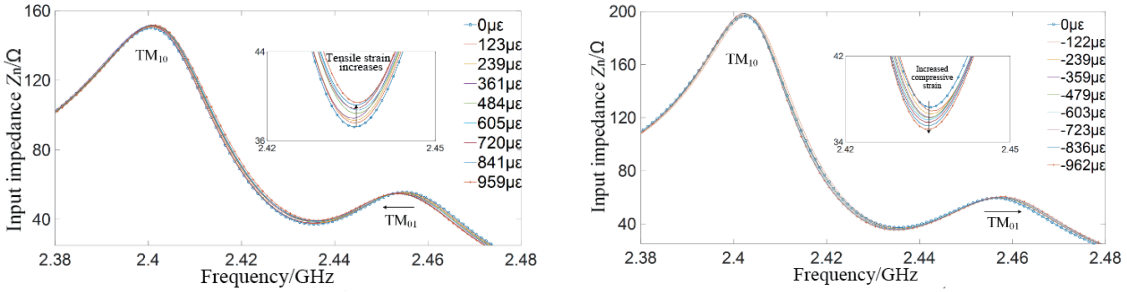

(a) (b)

Fig. 7. (Color online) Input impedances of MPAS under various *x*-direction strains: (a) tensile and (b) compressive.

TM_{10} mode shows no significant change, whereas the resonant frequency f_{01} corresponding to the TM_{01} mode shifts to the left, and Z_{min} increases. Figure 7(b) illustrates that as compressive strain increases, the f_{10} corresponding to the TM_{10} mode shows no significant change, whereas the f_{01} corresponding to the TM_{01} mode shifts to the right, and Z_{min} decreases.

Figure 8 shows the Z values of the MPAS under different y-direction strains. The total opposite phenomena can be found compared with those in Fig. 7.

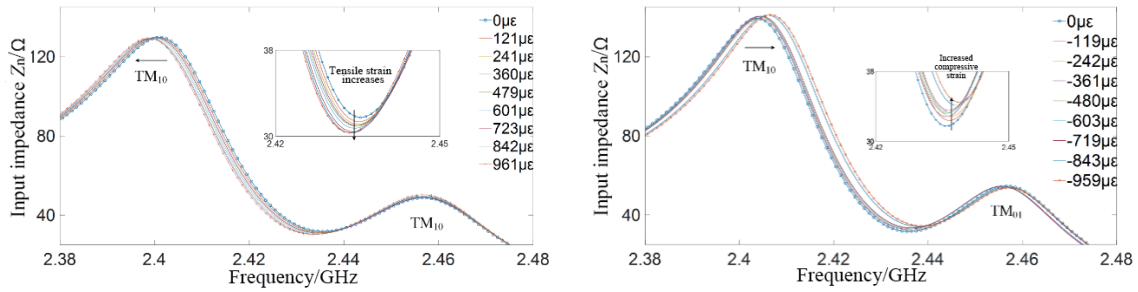

(a) (b)

Fig. 8. (Color online) Z values of MPAS under various y-direction strains: (a) tensile and (b) compressive.

To minimize random test errors, 10 repeated experiments were conducted for each strain level in each test group. Tables 2 and 3 present the average strains and average Z_{min} values from the 10 repeated experiments. The theoretical strain and normalized Z_{min} average (Z_n) in the tables are calculated using Eqs. (7) and (8), respectively.

$$\varepsilon = \frac{\sigma}{E} = -\frac{My}{EI_z} = \frac{6mg(L-d)}{Ebt^2} \tag{7}$$

$$Z_n = \frac{Z_{min} - Z_{min0}}{Z_{min0}} \times 10^6 \tag{8}$$

It is evident that the Z_{min} variations of the MPAS at the corresponding f_{10} or f_{01} accurately reflect the strain of the aluminum beam. When the f_{01} of the TM_{01} mode shifts, the strain direction is determined as the x-direction: a leftward shift of f_{01} combined with an increase in Z_{min} indicates tensile strain in the beam, whereas a rightward shift of f_{01} with a decrease in Z_{min} indicates compressive strain. When the f_{10} of the TM_{10} mode shifts, the strain direction is determined as the y-direction: a leftward shift of f_{10} combined with a decrease in Z_{min} indicates tensile strain, whereas a rightward shift of f_{10} with an increase in Z_{min} indicates compressive strain.

As shown in Fig. 9, the experimental ε_xs and ε_y values in Tables 2 and 3 are well linearly fitted with Z_n; the fitting equation for Z_n versus ε_x is $Z_n = 59\varepsilon_x + 1839$, with goodness of fit R^2 of 0.994. The strain sensitivity in the x-direction (GF_x) of the MAPS is 59 ppm/με. The fitting equation for Z_n versus ε_y is $Z_n = -71\varepsilon_y + 9538$, with goodness of fit R^2 of 0.973. The strain sensitivity in the y-direction (GF_y) of the MAPS is −71 ppm/με, with the negative sign confirming the inverse relationship between Z_n and ε_y. It can be seen that since the strains in the x- and y-directions correspond to the modal changes of the MPAS in the two directions, the curves in the two figures are not symmetric.

The linearity (δ) of the MPAS, a key metric describing the static characteristics of the sensor, is calculated as

Table 2
Average strain in *x*-direction, Z_{min}, and their standard deviations of MPAS.

Theoretical ε_x (με)	Average experimental ε_x (με)	Experimental Z_{min} (Ω)	Normalized Z_n (ppm)	Standard deviation of experimental ε_x (με)	Standard deviation of experimental Z_{min}
−960	−961.5	35.2	−54672.4	0.7	0.0239
−840	−836.1	35.5	−45546.6	0.4	0.0228
−720	−723.4	35.8	−37088.2	1.2	0.0214
−600	−603.2	36.1	−30984.0	0.6	0.0282
−480	−478.8	36.2	−26240.9	0.8	0.0245
−360	−359.4	36.3	−25130.8	0.1	0.0205
−240	−239.4	36.6	−16668.3	0.5	0.0239
−120	−122.4	36.9	−8920.6	1.1	0.0268
0	0.0	37.2	0	0.7	0.0272
120	123.4	37.6	9800.4	0.2	0.0258
240	238.7	37.8	15755.1	0.8	0.0316
360	361.1	38.0	21098.8	0.9	0.0257
480	483.5	38.5	32751.6	0.6	0.0261
600	604.6	38.7	41258.1	0.2	0.0283
720	720.4	38.9	44248.3	0.3	0.0289
840	841.4	39.2	53045.7	1.6	0.0227
960	959.1	39.4	59023.2	1.1	0.0313

Table 3
Average strain in *y*-direction, Z_{min}, and their standard deviations of MPAS.

Theoretical ε_x (με)	Average experimental ε_x (με)	Experimental Z_{min} (Ω)	Normalized Z_n (ppm)	Standard deviation of experimental ε_x (με)	Standard deviation of experimental Z_{min}
−960	−959.4	34.5	85877.9	0.8	0.0135
−840	−842.6	34.1	74491.3	0.3	0.0259
−720	−719.1	33.5	55872.8	0.8	0.0168
−600	−602.6	33.3	49227.1	0.7	0.0140
−480	−480.4	33.2	46584.1	0.4	0.0226
−360	−361.2	32.9	33402.1	1.1	0.0183
−240	−241.6	32.8	35165.8	0.8	0.0146
−120	−118.9	32.3	19792.1	0.5	0.0186
0	0.0	31.7	0	0.2	0.0164
120	121.2	31.4	−7993.1	0.5	0.0227
240	240.5	31.1	−19745.9	0.7	0.0179
360	359.8	31.0	−22974.9	0.8	0.0195
480	478.5	30.9	−24729.9	1.2	0.0247
600	601.2	30.7	−31871.0	0.8	0.0148
720	722.6	30.5	−41610.5	0.2	0.0226
840	842.3	30.4	−45091.5	0.8	0.0255
960	961.4	30.3	−44375.7	0.1	0.0223

$$\delta = \frac{\Delta Z_{max}}{Z_{fs}} \times 100\% , \tag{9}$$

where ΔZ_{min} is the gap between the measured and fitted values of Z_n, and Z_{fs} is the maximum Z_n.

The stability (δ_s) of the MPAS is defined as the ratio of the maximum deviation among repeated measurements to the full-scale range of the sensor, and calculated as

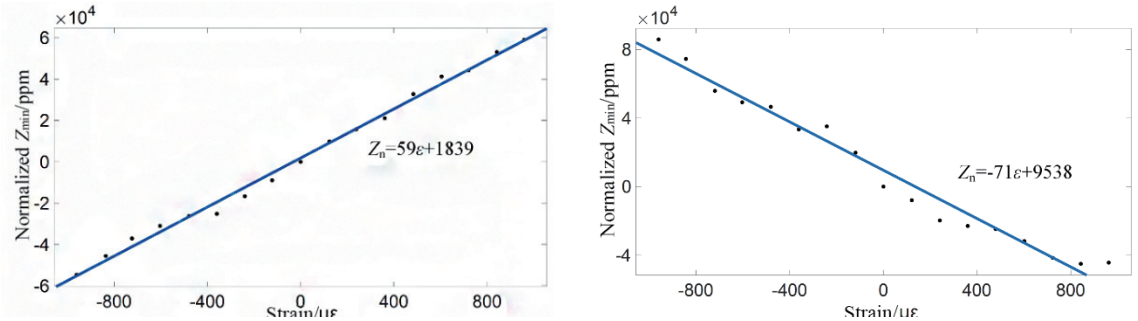

(a) (b)

Fig. 9. (Color online) Fitting curves of Z_n and ε of MPAS: (a) x- and (b) y-directions.

$$\delta_s = \frac{\Delta Z}{FSR} \times 100\%, \tag{10}$$

where ΔZ is the maximum deviation of Z in 10 repeats under the same strain condition and FSR is the full-scale range of the MPAS. Here, the calculated δ and δ_s of the MPAS are 24 and 2.6%, respectively, which are superior to those of conventional strain sensors.

4.2 Strain sensing performances with reflection coefficient

The reflection coefficient (S_{11}) values of the MPAS subjected to tensile and compressive ε_x are shown in Figs. 10(a) and 10(b), respectively. As tensile ε_x increases, the high-frequency minimum f_3 of S_{11} shifts to the left, the low-frequency minimum f_1 remains virtually unchanged, and the maximum S_{11} shifts downward. When compressive ε_x increases, the high-frequency minimum f_3 of S_{11} shifts to the right, the low-frequency minimum f_1 remains virtually unchanged, and the maximum S_{11}shifts upward.

Figure 11 shows the S_{11}s of the MPAS under different ε_y values. The total opposite phenomena can be found as compared with those in Fig. 10.

Clearly, the S_{11} variations of the MPAS also effectively reflect the strains of the aluminum beam. If the high-frequency minimum f_3 of S_{11} shifts, the strain direction is identified as the x-direction: A leftward shift of f_3 combined with a downward shift of S_{11} at f_2 indicates tensile strain in the beam. Conversely, a rightward shift of f_3 with an upward shift of S_{11} at f_2 indicates compressive strain. If the low-frequency minimum f_1 of S_{11} shifts, the strain direction is identified as the y-direction: A leftward shift of f_1 combined with an upward shift of S_{11} at f_2 indicates tensile strain. Conversely, a rightward shift of f_1 with a downward shift of S_{11} at f_2 indicates compressive strain.

As shown in Fig. 12, the experimental ε_x and ε_y are also linearly fitted with S_{11}, and the fitting equations in the x- and y-directions are $S_{11} = 141\varepsilon_x + 16520$ ($R^2 = 0.978$) and $S_{11} = -140\varepsilon_y + 16710$ ($R^2 = 0.979$), and the corresponding GF_x and GF_y are 141 and 140 ppm/με, respectively.

Similar to the Z_{min} characterization method, the calculated δ and δ_s of the MPAS based on the S_{11} sensing method are 18 and 2.0%, respectively.

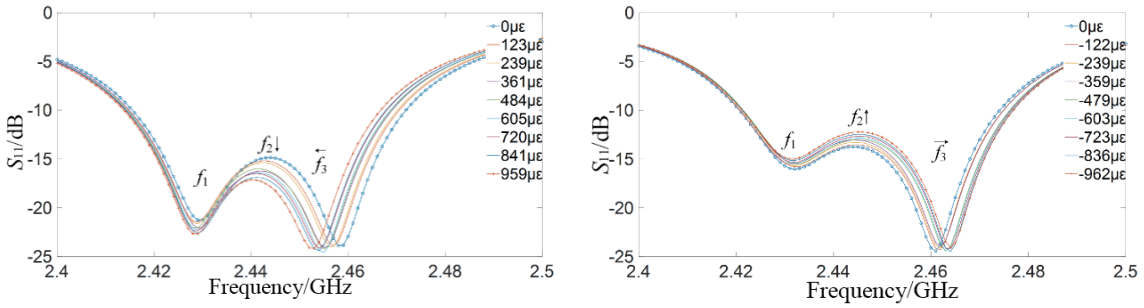

(a) (b)

Fig. 10. (Color online) S_{11} values of MPAS under different ε_x values: (a) tensile and (b) compressive.

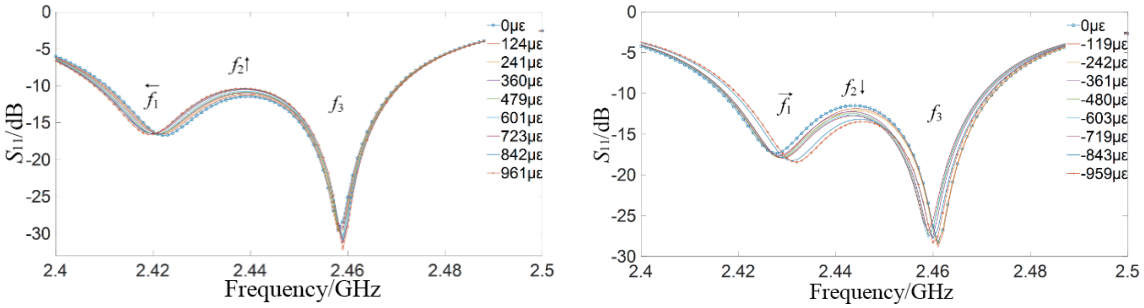

(a) (b)

Fig. 11. (Color online) S_{11} values of MPAS under different ε_y values: (a) tensile and (b) compressive.

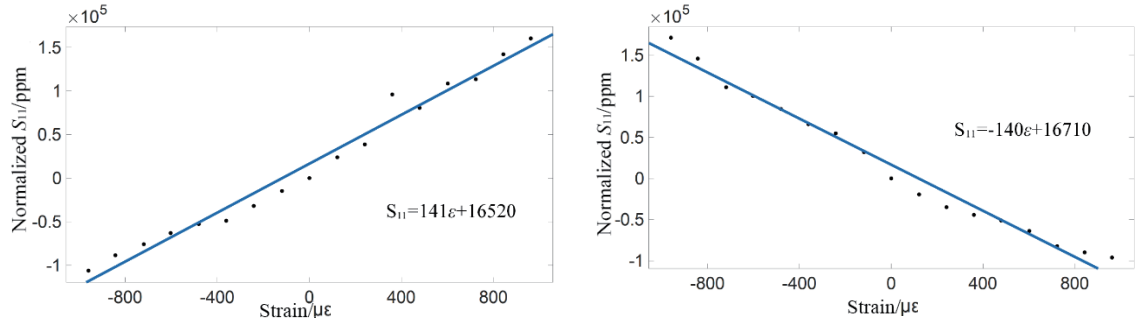

(a) (b)

Fig. 12. (Color online) Fitting curves of normalized S_{11} and ε of MPAS: (a) x- and (b) y-directions.

5. Conclusions

The MPAS with a slotted design for circular polarization achieves bidirectional strain monitoring with high sensitivity, excellent stability, and goodness of fit. Conclusions are derived as follows.

Slotting at appropriate positions on the MPA enables circular polarization. When two slots (2.5 mm length × 1.5 mm width) are symmetrically cut on both sides of a 40 mm × 40 mm radiation patch, the sensor generates two orthogonal modes (TM_{10} and TM_{01}) with resonant

frequencies at f_{10} = 2.402 GHz and f_{01} = 2.458 GHz, respectively. This configuration can realize bidirectional strain monitoring. The MPAS can cooperatively characterize structural strain through Z_{min} and S_{11}.

When the frequency f_{10} corresponding to the TM_{10} mode does not shift and the frequency f_{01} corresponding to the TM_{01} mode shifts, the strain is in the x-direction. The fitting curve between Z_n and ε_x is $Z_n = 59\varepsilon_x + 1839$ with GF_x of 59 ppm/με and goodness of fit R^2 of 0.994. Similarly, the obtained fitting curve is $Z_n = -71\varepsilon_y + 9538$ with GF_y of −71 ppm/με and goodness of fit R^2 of 0.973.

When the high-frequency minimum f_3 of S_{11} shifts while the low-frequency minimum f_1 of the S_{11} remains unchanged, the structural strain is in the x-direction. The fitting curve between the normalized S_{11} and ε_x is $S_{11} = 141\varepsilon_x + 16520$ with GF_x of 141 ppm/με and goodness of fit R^2 of 0.978. Similarly, the obtained fitting curve is $S_{11} = -140\varepsilon_y + 16710$ with GF_y of −140 ppm/με and goodness of fit R^2 of 0.979.

Note that experimental observations reveal significant impacts on sensor performances due to the temperature sensitivity of radiation patch dimensions and the humidity sensitivity of the dielectric substrate. We will focus on designing moisture-resistant packaging structures and establishing temperature-humidity calibration models to further optimize the environmental stability of the MPAS for strain monitoring.[33]

Acknowledgments

This study was financially supported by the Natural Science Foundation of China (51878364), the Natural Science Foundation of Shandong Province (ZR2023ME011), and the National 111 Program, Shandong Provincial Peak Discipline Funding.

References

1 M. Naresh, V. Kumar, J. Pal, S. Sikdar, S. Banerjee, and P. Banerji: Smart Mater. Struct. **33** (2024) 7. https://doi.org/10.1088/1361-665X/ad5504
2 S. Ahmed, E. T. Thostenson, T. Schumacher, S. M. Doshi, and J. R. McConnell: Compos. Struct. **203** (2018) 182. https://doi.org/10.1016/j.compstruct.2018.07.005
3 X. Q. Yang: Research on Antenna Sensors for Metal Crack State Monitoring[D]. Chongqing University (2022) (in Chinese). https://doi.org/10.27670/d.cnki.gcqdu.2022.001313
4 A. R. C. Vasconcelos, R. A. de Matos, M. V. Silveira, and E. Mesquita: Buildings **14** (2024) 8. https://doi.org/10.3390/buildings14082345
5 Y. H. Lu: Research on the Design of Active Layer Structure and Piezoresistive Performance Based on Graphene and MXene[D]. Beijing University of Chemical Industry (2023) (in Chinese). https://doi.org/10.26939/d.cnki.gbhgu.2023.000074
6 H. Jiang, J. Zhang, M. Qin, J. B. Zhang, X. T. Zou, and X. Weng: Sens. Actuators, A **356** (2023) 114359. https://doi.org/10.1016/j.sna.2023.114359
7 Z. P. Zhang: Research on Concrete Damage Monitoring Based on Embedded Piezoelectric Sensors[D]. Chongqing Jiaotong University (2024) (in Chinese). https://doi.org/10.27670/d.cnki.gcqdu.2022.001313
8 S. Jiang, Y. Shen, S. L. Wang, W. Jiang, Y. Liu, and Q. Z. Wu: Sens. Actuators, A **362** (2023) 114655. https://doi.org/10.1016/j.sna.2023.114655
9 H. C. Yu, C. L. Cheng,P. H. Wu, and S. J. Li: Sens. Mater. **29** (2017) 7. https://doi.org/10.18494/SAM.2017.1545
10 W. H. Zhang, G. Q. Gu, H. X. Ren, Z. H. Zhang, Z. Y. Zhang, H. F. Qin, M. L. Zheng, Z. L. Du, and G. Cheng: Nano Energy **136** (2025) 110729. https://doi.org/10.1016/j.nanoen.2025.110729

11 H. E. Joe, H. Yun, S. H. Jo, M. B. G. Jun, and B. K. Min: Int. J. Precis. Eng. Manuf. Green Technol. **5** (2018) 1. https://doi.org/10.1007/s40684-018-0017-6
12 J. Y. Lin, J. H. Chen, and K. H. Chen: Sens. Actuators, A **193** (2013) 233. https://doi.org/10.1016/j.sna.2013.01.044
13 S. L. Yang, K. J. Xu, Z. P. Shu, and W. Xu: Electron. Meas. Instrum. **30** (2016) 9 (in Chinese). https://doi.org/10.13382/j.jemi.2016.09.010
14 X. P. Li, H. L. Dong, S. Z. Zhu, T. Liu, H. Y. Wang, and Y. Y. Niu: Micronanoelectronic Technol. **59** (2022) 12 1243–1250+1329 (in Chinese). https://link.oversea.cnki.net/doi/10.13250/j.cnki.wndz.2022.12.001
15 J. Yu: Research on Comprehensive Design Theory and Key Technologies of Microstrip Patch Antenna Mode [D]. Nanjing University of Posts and Telecommunications (2022) (in Chinese). https://doi.org/10.27251/d.cnki.gnjdc.2022.000040
16 S. Todi and P. Agarwal: Biomed. Eng. Lett. **15** (2025) 249. https://doi.org/10.1007/s13534-024-00443-7
17 K. F. Lee and K. F. Tong: Proc. IEEE. **100** (2012) 2169. https://doi.org/10.1109/JPROC.2012.2183829
18 R. Xue, Y. Kuang, and B. F. Gu: Dyeing & Finishing Technol. **46** (2024) 4 (in Chinese).
19 J. Q. Zhang, C. Li, Y. Gao, J. P. Tan, F. Z. Xuan, and X. F. Ling: Sens. Actuators, A **347** (2022) 113960. https://doi.org/10.1016/j.sna.2022.113960
20 C. F. He, T. T. Yan, G. R. Song, Y. Lv, and B. Wu: Chinese J. Sci. Instrum. **38** (2017) 2 (in Chinese). https://doi.org/10.19650/j.cnki.cjsi.2017.02.013
21 H. Y. Ge, H. Li, Y. L. Chen, M. B. Liu, and Q. Y. Wang: Scientia Sinica Technologica **44** (2014) 9 (in Chinese)
22 P. Lopato and M. A. Herbko: Sensors **18** (2018) 1. https://doi.org/10.3390/s18010310
23 C. X. Xu, Y. H. Wang, Y. F. Li, H. Cai, and G. D. Han: Sens. Mater. **35** (2023) 10. https://doi.org/10.18494/SAM4598
24 X. Z. Li, S. T. Xue, L. Y. Xie, L. Pang, G. C. Wan, and R. S. Li: J. Build. Eng. **94** (2024) 109931. https://doi.org/10.1016/j.jobe.2024.109931
25 S. Weng, J. Zhang, K. Gao, H. Zhu, and T. J. Peng: Sensors **24** (2024) 13. https://doi.org/10.3390/s24134388
26 Z. Y. Wu: Research on implementation methods of broadband circularly polarized antennas [D]. Xi'an University of Posts and Telecommunications (2023) (in Chinese). https://doi.org/10.27712/d.cnki.gxayd.2023.000046
27 K. R. Jha and G. Singh: J. Comput. Electron. **9** (2010) 1. https://doi.org/10.1007/s10825-009-0297-8
28 A. F. Tinoco, D. C. Nascimento, R. Schildberg, and J. C. D. Lacava: IEEE Antennas Propag. Mag. **53** (2011) 1. https://doi.org/10.1109/MAP.2011.5773598
29 G. R. Song, X. D. Wang, Y. Lv, T. T. Sun, S. Wang, J. Ren, C. F. He, and B. Wu: J. Beijing University of Technol. **45** (2019) 1 (in Chinese). https://doi.org/10.11936/bjutxb2017080041
30 C. F. Chen, L. Zou, C. L. Bi, and A. D. Wang: Sensors **24** (2024) 23. https://doi.org/10.3390/s24237608
31 L. Y. Sun: Research on decision support for automatic positioning and tracking technology selection in construction[D]. Dalian University of Technology (2011) (in Chinese).
32 L. L. Wang, K. L. Chung, S. Gao, M. L. Ma, J. L. Luo, and Y. S. Li: Appl. Comput. Electromagn. Soc. J. **36** (2021) 9. https://doi.org/10.47037/2021.ACES.J.360917
33 R. Zeiser, T. Fellner, and J. Wilde: J. Sens. Sens. Syst. **3** (2014) 1. https://doi.org/10.5194/jsss-3-77-2014

About the Authors

Liu Liguang received his B.S. degree in civil engineering from Beihua University in 2024. Currently, he is pursuing a master's degree in civil and hydraulic engineering at Qingdao University of Technology, with research focusing on smart materials and structures. (liuliguang@stu.qut.edu.cn)

Jianlin Luo received his M.S. degree in structural engineering in 2005 and his Ph.D. degree in engineering mechanics in 2009 from Harbin Institute of Technology. In December 2009, he joined the School of Civil Engineering, Qingdao University of Technology, Qingdao (QUT). He was appointed as an associate professor in 2012 and a full professor in 2023 at QUT. He was a Visiting Scholar at Monash University, Melbourne from 2015 to 2016 and a Visiting Fellow at Western Sydney University, Sydney, Australia from 2018 to 2019. He has authored and coauthored over 100 journal papers, and held 20 invention patents. His current research interests include smart materials and structural health monitoring, advanced construction materials, and applications in infrastructure. (lawjanelim@qut.edu.cn)

Kwok L. Chung received his Ph.D. degree from Sydney University of Technology, Australia, in 2004. He is a senior member of IEEE and is currently a research professor in Guangzhou Institute of Technology. His current research interests include passive wireless sensors, cement-based materials design and characterization, microwave antennas, and metasurface. He is the Founding Chair of the IEEE Qingdao AP/MTT/COM joint chapter (CN10879) under the Beijing Section. He serves as a reviewer for numerous IEEE, IET, Elsevier, and other international journals. (klchung@gzist.edu.cn)

Yang Liu received his M.S. degree in structural engineering in 2004 and his Ph.D. degree in engineering mechanics in 2008 from Harbin Institute of Technology (HIT). He joined the School of Transportation Science and Engineering in HIT. He was appointed as an associate professor in 2012 and a full professor in 2020 at HIT. His research interests are in smart materials and structural health monitoring. (ly7628@hit.edu.cn)

Aiqi Cui received her B.E. degree in packaging engineering from Hunan University of Technology in 2016 and her master's degree in material science and technology from Qingdao University of Technology in 2019. Her research interests include electromagnetic shielding, material characterization, and artistic antennas. (18873375230@139.com)